Nuclear Instruments and Methods in Physics Research B 269 (2011) 69–81

Contents lists available at ScienceDirect

Nuclear Instruments and Methods in Physics Research B

journal homepage: www.elsevier.com/locate/nimb

A GUPIX-based approach to interpreting the PIXE-plus-XRF spectra from the Mars Exploration rovers: II geochemical reference materials ☆

J.L. Campbell [a,*], A.M. McDonald [b], G.M. Perrett [a], S.M. Taylor [c]

[a] Guelph-Waterloo Physics Institute, University of Guelph, Guelph, Ontario, Canada N1G 2W1
[b] Department of Earth Sciences, Laurentian University, Sudbury, Ontario, Canada P3E 2E6
[c] Department of Atmospheric and Oceanic Sciences, McGill University, Montréal, Québec, Canada H3A 2T5

ARTICLE INFO

Article history:
Received 22 July 2010
Available online 12 November 2010

Keywords:
Particle-induced X-ray emission analysis
X-ray fluorescence analysis
Alpha particle X-ray spectrometer
Calibration
Geochemical reference materials

ABSTRACT

A detailed examination of the original calibration data for the laboratory version of the Mars Exploration Rover alpha particle X-ray spectrometer is undertaken to ascertain if the results from a suite of certified geochemical reference materials (GRMs) agree with the APXS calibration based upon homogeneous standards which was established in the previous paper. Various discrepancies, some of them large, are observed for specific elements in specific rock types, and it is argued on the basis of X-ray diffraction analyses of the GRMS that these are caused by the mineral phase structure of the rocks. Elements present in accessory mineral phases can be subject to very large errors, necessitating caution in interpretation of trace element results from the APXS. Some of the discrepancies can be dealt with by developing sub-calibrations, each of which is "tuned" to a specific rock type. This approach has the potential to provide more accurate APXS analysis of unknown rocks than a calibration scheme based upon a simple averaging over many rock types within a GRM suite, or over a mix of rock and homogeneous standards. It also has the potential to measure the content of mineralogically bound water provided that a means of determining the distance from sample to detector is available.

1. Introduction

In the preceding paper [1] (referred to below as Part I), a new calibration method was applied to the laboratory model of the Mars Exploration Rover (MER) alpha-particle X-ray spectrometers (APXS). The method was based upon a fundamental physics approach to the determination of the matrix terms in the equation which relates observed X-ray intensity from an element in a sample to the concentration of that element. These important terms account rigorously for the X-ray producing interactions undergone by the exciting alpha particles and plutonium L X-rays within the specimen, and for the subsequent transmission of the excited characteristic X-rays out of the specimen.

Gellert et al. [2] list the extensive primary suite of standards (including pure elements, simple chemical compounds and geochemical reference materials) which they used to establish the earlier, partly empirical calibration upon which the entire published set of Martian rock and soil analyses from the Spirit and Opportunity rovers [3] has been based. They also recorded spectra from a secondary group of standards which lacked certification by bodies such as national laboratories or geological surveys. We deliberately restricted ourselves in Part I to a subset of the primary suite comprising only pure elements and simple chemical compounds, for which we had strong assurance of homogeneity of elemental distribution at the sub-micron scale within the sample matrix; the geochemical reference materials (GRMs) were excluded. However, we were able to show that certain minerals from Gellert's secondary suite were very close to being a single phase, and their addition to the calibration provided a significant improvement in its credibility. Our restriction to homogeneous materials within the definition given above assured us that both the exciting radiation and the excited characteristic X-rays arising from an interaction at any location within the sample would be subject to precisely the same matrix effects apart from specifics of the geometry.

Use of GRMs for calibration of an analytical instrument is considered highly desirable in the geochemical community because of the greater resemblance that they bear to real rock samples as compared to the simpler homogeneous standards used by us in Part I. But these GRMs bring significant new issues, because rocks may be composed of multiple mineral phases and may then violate the assumption of homogeneous elemental distribution that was

☆ Based in part on invited talks delivered at the Nineteenth International Conference on Ion Beam Analysis, Cambridge, UK, 2009 and at the Twelfth International Conference on PIXE and its analytical applications, Guildford, UK, 2010.

* Corresponding author. Tel.: +1 519 824 4120x52325; fax: +1 519 836 9967.
E-mail address: icampbel@uoguelph.ca (J.L. Campbell).

0168-583X/$ - see front matter © 2010 Elsevier B.V. All rights reserved.
doi:10.1016/j.nimb.2010.09.014

demonstrably met in Part I. This reality was clearly acknowledged by Gellert et al. [2], but their calibration was done by an averaging process over the GRMs and the simple chemical standards, such that the effect of multiple mineral phases in the GRMs was not investigated in any detail.

It is precisely because of this mineral phase issue that X-ray fluorescence analysis of rocks for the major elements invariably includes a preliminary stage in which a lithium borate fusion process is employed to reduce the rock to a homogeneous, glassy material. Such a procedure is obviously impossible as far as the in situ analysis conducted on Mars is concerned, and so a detailed investigation of the influence of mineral phase effects is highly desirable. One might expect the light elements (sodium, magnesium, etc.), whose X-rays are excited by PIXE, to be more susceptible to these effects than the heavier elements (iron, zinc, etc.) whose X-rays are primarily excited by XRF. The depth probed by the ~5 MeV alpha particles is only a few microns, which makes it extremely likely that a given alpha particle would sample only a single phase. In such a case, the appropriate matrix term would reflect the element concentrations of that specific phase: but in both our approach and that of Gellert et al. [2] computation of the matrix terms is predicated on the assumption that the matrix is a homogeneous mixture (at the sub-micron scale) of the elements which are contributed by all the different phases. The propensity for error is thus obvious. In the longer term, there may be solutions for this problem, but our present task is simply to elucidate the details and propose empirical remedies.

In our earlier study [4] of the MER APXS standards data, we observed that the calibration results for sodium and aluminum in basalt GRMs differed markedly from those in other GRMs and homogeneous standards. This is a non-trivial observation, insofar as the Martian surface is predominantly basaltic [5]. We observed that these anomalies had an approximate linear dependence upon the silicate (SiO_2) content across the progression from basalts through andesites to rhyolites. This led to the idea of developing "sub-calibrations" based upon the position of an igneous rock within the widely used LeMaitre [6] classification scheme (Fig. 1) which assigns rocks to named regions within a plot of alkaline oxide versus silicate content. Recognizing the limited number and type of GRMs used in Ref. [3], we combined rock types in the lower region of the LeMaitre diagram to provide such sub-calibrations for three igneous rock types.

The main purpose of this paper is to examine the influence of mineralogy in greater breadth and depth. We shall investigate whether or not the GRM results agree with the calibration which we established in Part I, in order to ascertain if different rock types obey this calibration and to understand the reasons if they do not. To support this effort, we have conducted X-ray diffraction analysis of the mineralogy of each GRM. The reader will discern that we have modified our approach to the APXS calibration, by rigorously separating two distinct subsets of standards, viz. (i) the materials of Part I, and (ii) the GRMs studied here. In addition, both of these subsets have been expanded relative to our earlier work [4], where we restricted ourselves to those of Gellert's GRMs which were certified by a recognized national organization. To maximize the representation of each rock type, we have removed that restriction. Because typical APXS spectra were shown in the preceding paper, none will be shown here.

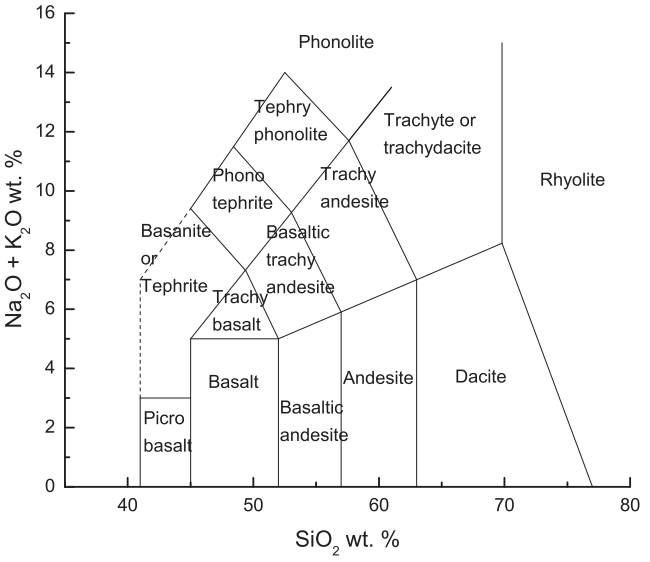

Fig. 1. LeMaitre diagram for classification of igneous rocks by total alkaline oxide to silicate (TAS) ratio.

2. The geochemical reference materials

The GRMs used here are listed in Table 1. In Ref. [4] we used the spectra from the 24 certified GRMs which are listed by Gellert et al. [2] within the overall 53 reference materials that were the basis of

Table 1
Geological reference materials supplied for the work of Ref. [2] by the Service d'Analyse des Roches et des Mineraux du CNRS (SARM), the US Geological Survey (USGS), the Japanese Geological Survey (JGS), the Max-Planck-Institüt fur Chemie (MPIC), and Natural Resources Canada (CANMET).

GRM	Supplier (C: certified, P: provisional)	Certificate description	Wt.% "X-ray invisible" H_2O+, CO_2, Li_2O, etc.
A:	Minerals		
AL-I	C: SARM	Albite	0.62
DT-N	C: SARM	Kyanite	1.52
FK-N	C: SARM	Feldspar	0.41
GL-O	C: SARM	Glauconite	5.58*
Mica-Fe	C: SARM	Biotite	3.36*
Mica-Mg	C: SARM	Phlogopite	2.26*
UB-N	C: SARM	Serpentine	11.23*
B: Igneous			
BE-N	C: SARM	Basalt	2.98
BR	C: SARM	Basalt	3.16
PM-S	C: SARM	Microgabbro	0.92
WS-E	C: SARM	Dolerite	1.42
AGV1	C: USGS	Andesite	0.81
BCR1	C: USGS	Basalt	0.78
DR-N	C: SARM	Diorite	2.32
I555	MPIC	Andesite	nd
SSK-1	MPIC	Andesite	nd
AC-E	C: SARM	Granite	0.29
GA	C: SARM	Granite	0.98
GH	C: SARM	Granite	0.76
GS-N	C: SARM	Granite	1.2
MA-N	C: SARM	Granite	2.26
AN-G	C: SARM	Anorthosite	0.74
ISH-G	P: SARM	Trachyte	nd
MDO-G	P: SARM	Trachyte	nd
SY-4	P: CANMET	Diorite	4.5
C:	Sediments		
Jsd2	C: JGS	Stream sed.	3.22
MAG1	C: UGS	Ocean sed.	13.68
D: Other			
BX-N	C: SARM	Bauxite	11.92*
GXR1	C: USGS	Jasperoid	4.37*

nd: not determined on certificate.
* See discussion in Section 7.3.

their calibration of the MER APXS. We included the hydrated phyllosilicate UB-N, for which Gellert et al. recorded spectra, although it was excluded from their final list. In our earlier work, we excluded the two trachytes ISH-G and M-DOG, because the supplier defined the element concentrations as "provisional". Here we find it useful to include these two materials because they exemplify some of the mineral phase issues mentioned above. We have supplemented our andesite data by adding the two Max-Planck-Institüt fur Chemie (MPIC) standards I555 and SSK1. And we have added two samples from a set of "blind" materials which were supplied to the MER APXS team by NASA's Jet Propulsion Laboratory. Identification of these materials has been provided to us by JPL [7]: one is a phonotephrite rock GRM, and the other conveniently duplicates one of Gellert's GRMs, thereby providing a valuable test of reproducibility.

The first rock group within our extended GRM subset comprises seven materials which are essentially mono-mineralic; one might expect that these will follow the calibration of Part I but this should not be assumed. Next, there is a large group of igneous rocks. Using Fig. 1, 15 of the GRMs fall within the bottom row of the LeMaitre diagram, ranging from picro-basalts to rhyolites. The two trachytes have silicate concentrations equivalent to andesites, but have much higher alkaline oxide levels. A similar remark applies to the tephrite SY-4 with respect to basalts. AN-G is predominantly composed of the mineral plagioclase feldspar; it does not fall within the scheme of Fig. 2, and, in fact, is close to mono-mineralic. The standards MAG-1 and Jsd-2 are sediments, of ocean-floor and stream-bed origin respectively. BX-N is bauxite, well known as an aluminum ore. GXR-1 is jasperoid, a highly altered rock comprising mainly quartz and hematite. Although the supplier describes the Mica-Fe GRM as biotite, the presence of both iron and magnesium indicates that it is intermediate within the phlogopite–annite series.

As indicated in Part I, the certified GRMs were received from their suppliers in powder form. The powders were sieved by Gellert et al. [2] to exclude grains over 75 μm in diameter, and then spread in a sample holder with care to achieve as smooth a surface as possible.

The certificates supplied with these GRMs indicate the presence, in many cases, of very small amounts (on average about 0.5 wt.%) of adsorbed water, denoted H_2O-. We assume here that pre-heating, followed by exposure to vacuum in the analysis chamber of Gellert et al. [2], has removed this water, and so we have renormalized the certificate concentrations of the remaining oxides to a total of 100 wt.%; this is a very small effect. Of significantly more consequence in the context of analysis on Mars is the presence in several cases of mineralogically bound water, denoted H_2O+, whose concentration can be quite large. Obviously, water cannot be detected directly by any X-ray emission technique. Other such "X-ray invisible components" in the GRMs and in natural samples are fluorine, nitrogen, and the oxides of lithium, boron and carbon. Examples of GRMs having significant X-ray invisible components, according to their certificates, are the phyllosilicate UB-N with 11.2 wt.% of bound water plus CO_2, and the ocean-floor mud MAG-1 with 13.7 wt.% of bound water plus CO_2.

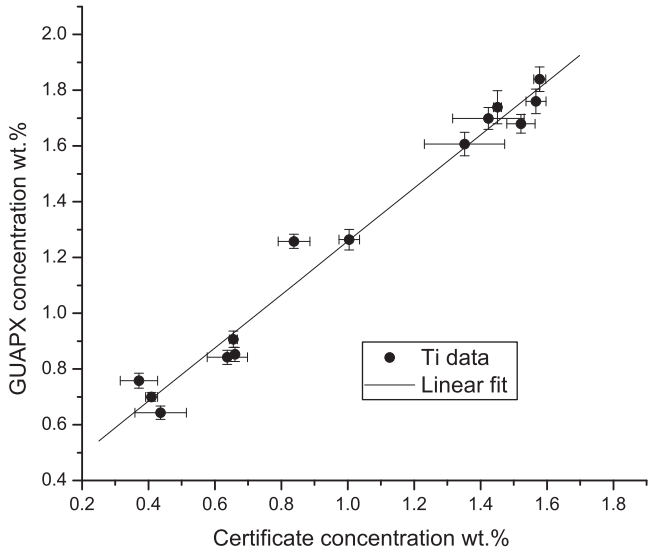

Fig. 2. Relationship between measured and certificate concentrations of titanium.

3. X-ray diffraction and Rietveld analyses of the GRMs

Samples of each GRM were front-loaded into an aluminum holder (diameter 25 mm) using a frosted glass slide. X-ray diffraction data were collected on a Philips PW 1710 $\theta - 2\theta$ system equipped with a diffracted-beam graphite monochromator, with a step size of 0.02°2θ and a counting time of 6 s/step over a range of 5–75°2θ. A fine-focus cobalt Kα X-ray tube was operated at 40 kV and 30 mA. Rietveld refinement analyses were carried out with Panalytical HighScore Plus version 2.2 software. Sources of the crystal-structure data for the constituent minerals are listed in Table 2. X-ray diffraction peaks were modeled using a pseudo-Voigt profile function with backgrounds being modeled using a six-order polynomial. The zero error, asymmetry (Rietveld), peak shape and cell parameters were refined for all phases. Preferred orientations of phases were corrected for using the method of March and Dollase [8,9]. For minerals present in abundances >5 modal%, refinement of atomic coordinates and site-occupancy factors (where appropriate) were conducted, while the compositions for those in less abundances were fixed at published values. No corrections for micro-absorption were applied. The quality of the difference between the calculated and observed diffraction profiles was evaluated using standard indices of agreement, the profile R-factor, R_p, the weighted profile R-factor R_{wp}, the expected R-factor, R_{exp}, and the goodness-of-fit index, S, as defined by Young et al. [28]. For minerals present in high abundances, the R_{Bragg} index was used as a qualitative guide to the goodness of fit. Relative errors in the modal abundances of the minerals analyzed are functions of concentration: based on the conditions under which the data were collected, for phases present in modal abundances greater than 10%, the typical relative error is 5%, with relative errors of 10–15% for those present in abundances of 5–10 modal%. Relative

Table 2
Sources of crystal-structure data for Rietveld refinements.

Mineral	Reference
Alkali feldspar	[10]
Analcime	[11]
Apatite	[12]
Biotite	[13]
Calcite	[14]
Chlorite	[15]
Clinoamphibole	[16]
Clinopyroxene	[17]
Gonnardite	[18]
Kyanite	[19]
Magnetite	[20]
Muscovite	[21]
Nepheline	[22]
Olivine	[23]
Plagioclase	[24]
Quartz	[25]
Rutile	[26]
Scapolite	[27]

Table 3
Mineralogy of GRMs as determined by Rietveld refinement of X-ray diffraction data: concentrations are in wt.%.

Mineral	BE-N	PM-S	WS-E	AGV2	BCR2	DR-N	ISH-G & MDO-G	AN-G
Plagioclase		64	58	70	69	51	86	93
K-feldspar			5	7		2		
Clinopyroxene	49	20	17	12	31		13	
Quartz			4	11		13	1	1
Magnetite	6	1				1		
Olivine	12	8						
Clinoamphibole		2.5	2			15		5
Biotite	1	1.5				5		
Chlorite		3.5	14			12		1
Apatite	2							
Gonnardite	11							
Nepheline	19							

	AC-E	GA	GH	GS-N	JSD-2	MAG1	DT-N	SY-4
Plagioclase	87	60	42	46	39	18		60
K-feldspar	6	18	26	24				
Clinopyroxene					34			
Quartz	7	14	27	19		16	2	2
Magnetite								1
Olivine								
Clinoamphibole				5	6			
Biotite				3				4
Chlorite		1	2	3	8	31	1	
Muscovite		7	3		13	34	1	
Kyanite							94	
Calcite						1		10
Rutile							2	
Analcime								2
Scapolite								21

errors increase rapidly for minerals present in concentrations less than 5 modal%, these typically being on the order of 100% for minerals present in concentrations below 0.5 modal%. The modal abundances are given in Table 3.

4. Formalism for elemental analysis by the APXS

It is worth repeating here that the method used rests upon the following equation from Part I, relating the observed yield $Y(Z)$ of a specific characteristic X-ray of a given element (atomic number Z) in a measurement of duration T seconds to its concentration C_Z:

$$Y(Z) = HC_ZTk(Z)F_{AP}(Z) \times [t_Z\varepsilon_Z]\left[M_{PIXE}(Z,\text{geom}) + \sum f_L M_{XRF}(Z,\text{geom})\right] \quad (1)$$

The first term on the right represents the expected intensity of X-rays from the PIXE process arising from the alpha particles emitted by the ^{244}Cm source, and the second term that of the X-rays from the XRF process induced by the various (hence the summation) plutonium L X-rays from the source. Computation of the terms denoted M, which describe the interactions of the ingoing and emerging radiations within the sample matrix, is based upon an atomic physics database which includes charged particle ionization cross-sections, photo-ionization cross-sections, ion stopping powers and X-ray attenuation coefficients. t_Z is the X-ray transmission fraction through any material interposed between the detector and the sample. ε_Z is the intrinsic efficiency of the detector. Finally, the factor $k(Z)$ provides a means for the user to introduce empirical corrections for specific elements in the event that the calibration exercise reveals defects in the database, detector characterization, etc. Until the calibration exercise is complete, $k(Z)$ is set as unity.

The matrix terms (sometimes called matrix corrections) can only be computed on the assumption that the elements of the sample or standard are uniformly distributed at the sub-micron level of distance. In the ion beam analysis context, an equivalent expression of this limitation is to require that the sample is "homogenous". (This use of the term should be distinguished from its other use, viz. that a small sample of a standard reference material should be fully representative of the initial bulk material.)

We perform a "fixed-matrix" (FM) solution of this equation. The matrix terms are computed by GUAPX from the known element concentrations. The H-value was determined from the homogeneous standards in Part I. The GUAPX program optimizes the fit to the spectrum, and deduces the values of C_Z for all elements observed in it. Those C_Z values are expressed as ratios $R(Z)$ relative to the stoichiometric or certificate concentration values; these ratios were accorded uncertainties by combining in quadrature the 2σ (two standard deviations) uncertainty of the fitted peak area and the 95% confidence level uncertainty in the certificate concentration. Note that this use of the symbol R is entirely distinct from its use in the XRD work of Section 3; it is consistent with our previous papers [1,4,29].

To a large extent, in our earlier study of the APXS calibration [4], we found reasonable consistency between the R-values from the group of simple chemical standards and those from the group of GRMs. However, for certain elements, systematic discrepancies were observed in the GRM data, which led us to a tentative, qualitative understanding of the effects of mineral phase heterogeneity in certain rock GRMs.

An appropriate first step in the present, extended study would be to analyze the subset of seven mono-mineralic GRMs using Eq. (1) in order to check if these data support the calibration of Part I. However, a full consideration of these results has to be delayed until the issue of spectrum artifacts that masquerade as X-ray contributions from elements in the standards is dealt with.

5. Correction for spectrum artifacts

A number of processes can contribute additional X-rays to the spectrum. These can augment the areas of the fitted X-ray peaks from elements in the sample, and hence also the deduced concentrations for various elements:

(i) Alpha and X radiation from the ^{244}Cm sources excite titanium K X-rays (4.51 and 4.93 keV) in the source cover foils, and some of these X-rays scatter from the sample into the detector; these scattered X-rays are indistinguishable from titanium K X-rays that originate from direct excitation within the sample.

(ii) Plutonium M X-rays from the sources are scattered by the sample into the detector; in the spectrum, the plutonium M lines (energies 3.35 and 3.76) overlap the K X-ray lines of potassium (3.31 and 3.59 keV) and calcium (3.69 and 4.01 keV) and cause a spurious increase in observed concentrations of these elements.

(iii) Zirconium K X-rays are excited via the photo-electric effect in the collimator by plutonium Lβ and Lγ X-rays which have scattered from the sample: the plutonium Lα X-rays have insufficient energy to contribute to this process. The intensity of the zirconium K X-rays in the spectrum is sufficient to preclude analysis for trace zirconium in geological materials.

(iv) Zirconium L X-rays arise via two processes. The first component arises in a simple manner from the atomic de-excitation cascades that follow emission of a zirconium K X-ray. The second component is due to photo-excitation in

the L-shell of zirconium atoms in the collimator by characteristic X-rays which arise in the sample but are intercepted by the collimator. The zirconium Lα X-ray line (energy 2.043 keV) overlaps the K line of phosphorus (energy 2.014 keV), and so the peak area of the latter is enhanced.

(v) A very small contribution of nickel K X-rays is attributed to scattered plutonium L X-rays interacting with a nickel-bearing component of the APXS.

(vi) A very small contribution of copper K X-rays is attributed similarly to scattered plutonium L X-rays interacting with the copper protective doors of the laboratory APXS instrument.

All of these six processes can result in "offsets" in the peak areas and hence in the concentrations of those elements whose X-rays cannot be distinguished from the artifact X-rays. The fluorescence of zirconium, nickel and copper will be enhanced if the instrument is placed within an external radiation field, as is the case with the Mars Exploration rovers, where the neighbouring Mössbauer instrument contains an intense source of the radionuclide ^{57}Co. The treatment of these effects thus becomes more complex in the case of the MER APXS analyses than it is for the terrestrial calibration.

In their paper on analysis of the GRM data set, Gellert et al. [2] tabulate the values of an average peak area offset (in counts per second) for each of titanium and potassium, while their tabulated offsets for phosphorus and copper are zero. These offset values are obviously unique to the terrestrial calibration geometry. When the instrument is on Mars, and the instrument-sample geometry changes from one sample to the next, the offset counting rate will obviously change. Thus a means of normalizing the calibration offset value for each specific Martian site is needed. In their terrestrial calibration, the measured element concentrations are converted by stoichiometry to oxide concentrations and their total is normalized to be 100 wt.%. In any other geometry, the oxide totals will be greater or less than 100 wt.%. If the assumption is made that for any Martian measurement, geometry is the sole reason for an observed departure from a 100 wt.% oxide total, then the ratio of the Martian oxide sum to the 100 wt.% terrestrial value can be used to normalize all individual Martian oxide concentrations to their proper value. This factor, referred to by Gellert et al. as the Geometric Norm, is used to normalize the area offsets of titanium and potassium. An unavoidable disadvantage of this procedure is that it precludes using any observed departure from 100 wt.% oxide total to infer the presence of "X-ray invisible" components, such as water or ice, in the Martian sample. Gellert et al. [2] also reported some negative area offsets, which they attributed to the fact that the relationship between peak area and element concentration for the lightest elements is quadratic rather then linear, as has been demonstrated by our Monte Carlo simulations [30].

In our approach, the focus is on concentrations rather than on peak areas, and so the concentration offsets are determined by plotting the measured concentration from GUAPX versus the certificate concentration. This has the disadvantage that the matrix calculations are applied to the entire peak area, whereas the reality is that these corrections are not appropriate for the artifact X-rays. But, given the smallness of the offset corrections, this is a minor issue. In common with the Gellert et al. [2] approach, we ignore the fact that those offsets which arise from scatter of radiation off the sample must have a dependence on the elemental composition of the sample. This neglect is justified by both the smallness of the offset corrections and the complexity that a fuller treatment would demand. An example is given in Fig. 2, and our offset values are listed in Table 4. They are close to the values that we calculated in our earlier treatment [4]. Our phosphorus concentration offset, previously 0.02%, is now revised to zero, reflecting a more rigorous assessment of the difficulty of determining the area of the weak phosphorus peak superposed on the flank of the intense neighboring silicon peak. In Part I, where we were dealing with high concentrations of the elements concerned, the effect of all these offsets was negligible.

Table 4
Concentration offsets.

Element	Offset
Ti	0.30 wt.%
K	0.12 wt.%
Ca	0.15 wt.%
Ni	20 ppm wt.
Cu	14 ppm wt.

On Mars, the sample-instrument distance varies, and so the offsets determined for the terrestrial calibration geometry must be corrected accordingly. At each iteration of the element concentrations, the total oxide concentration is compared to the 100 wt.% value pertaining in the terrestrial geometry, and the ratio is used to normalize the offsets to the geometry of the case at hand.

6. Consolidation of the fixed-matrix calibration using mono-mineralic GRMs

Each of the first seven GRMs listed in Table 1 appears from our XRD results to comprise essentially a single mineral. It follows that these GRMs should support and extend the calibration that we established in Part I through use of simple and homogenous standards. Table 5 permits comparison of their mean R-values with those of the homogeneous standards. For the latter, the quoted uncertainties are approximately half the range of the observed R-values. For the former, where there is sometimes a much greater spread in the error estimates from individual spectrum fits, they are, with two exceptions, the standard deviations; the exceptions are silicon and iron, where the number of GRMs is large enough and the spread of the results small enough that use of the error-weighted mean and its estimated error (EEM) appears to be justified.

We consider silicon first, because it gives the most intense X-ray peak in all the GRM spectra. For the seven mono-mineralic GRMs, the weighted mean $R_{wm} = 0.989 \pm 0.025$ (EEM), is in excellent agreement with Part I. The silicon K X-rays are excited almost entirely by PIXE, while, in contrast, more than 90% of the iron K X-rays are excited by XRF. The very good agreement of mean R-values between silicon and iron suggests that both the ratio between L X-ray and alpha particle intensities from ^{244}Cm and the ratio of excitation cross-sections for PIXE and XRF in our database are accurate. Calcium is the major element for which the two excitation processes are most closely balanced, and so it is unfortunate that we do not have data from the mono-mineralic GRMs to compare with the R-value of 1.005 for the chemical standards. However, the excellent results for potassium assure us that we continue to have good outcomes in this region of atomic number.

The case of aluminum is interesting. Two factors may justify deleting the highly anomalous UB-N result from further consideration; there is large uncertainty in the certified aluminum concentration, and aluminum in UB-N poses difficulty to the spectrum fitting program, with its peak sandwiched between peaks of magnesium and silicon that are fifteen times higher. While the mean R-value over the remaining six GRMs is in quite good agreement with the result from Part I, the individual data appear to fall into two sub-groups. The first sub-group comprises the feldspars AL-I and FK-N together with the nesosilicate kyanite (DT-N), for which R_m is 1.00 ± 0.03 (sd). The second group comprises the three phyllosilicates mica-Fe, mica-Mg and glauconite (GL-O), whose mean result of 0.91 ± 0.02 (sd), is lower,

Table 5
Comparison of mean *R*-values (R_m) for elements in the homogenous standards and the mono-mineralic GRMs. For the homogeneous standards, the uncertainty in R_m is taken as half of the range of measured individual values. For the GRMs, we define major elements (denoted M) as those having concentration $C > 1\%$, minor (denoted m) as $C \sim 0.1$–1%, and trace (denoted t) as $C < 0.1\%$. The quoted uncertainty in the mean *R*-value for a GRM is its standard deviation, except for the cases of Si and Fe where the standard error of the mean is used. In every case an additional uncertainty of ~2% from sample position variation is estimated.

Z	Homogeneous standards		Mono-mineralic GRMs		
	Number	R_m	Number and (M, m, t)	R_m	Range of individual error estimates
11	6	0.88 ± 0.05	2 (M)	0.95 ± 0.03	2–8%
12	3	0.96 ± 0.04	4 (M,m)	0.84 ± 0.05	1.7–4%
13	5	1.01 ± 0.03	6 (M)	0.97 ± 0.06 [b]	1.6–3.8%
14	7	1.01 ± 0.02	7 (M)	0.989 ± 0.025 [a]	1.1–1.8%
15	3	0.88 ± 0.015	0		
16	3	0.94 ± 0.03	0		
17	2	0.97 ± 0.015	4 (m,t)	1.29 ± 0.06	7–26%
19	1	0.99	4 (M)	0.99 ± 0.04	1.9–2.3
20	5	1.013 ± 0.01	0		
22	1	1.004	3 (m)	0.91 ± 0.15	3–6%
24	1	1.034	2 (t)	1.1 ± 0.13	6–17%
25	1	1.011	3 (m)	1.09 ± 0.05	6–13%
26	3	1.006	4 (M,m)	1.00 ± 0.016 [a]	1.4–4
28	2	0.99	4 (m,t)	1.06 ± 0.18	5–38%
29	1	0.975	0		
30	1	1.053	3 (m,t)	1.04 ± 0.01	7–15%
31	0		3 (t)	0.96 ± 0.02	14–17%
35	3	0.988			

[a] In these two cases the uncertainty estimate is the standard error of the weighted mean.
[b] Minor element in UB-N was low outlier and hence excluded.

as is seen later in Fig. 6. The difference may suggest some influence of the sheet structure of the phyllosilicates, which contain significant concentrations of bound water.

The mono-mineralic GRMs which provide magnesium data are all phyllosilicates (UB-N, GL-O, Mica-Fe, and Mica-Mg), and all display *R*-values well below the expectation from Part I. It is unfortunate that we have no framework or other silicate types to compare with. We do observe that decreasing *R*(Mg) correlates with increasing iron concentration, which might suggest that the possibility of a problem in the database with the attenuation coefficients for magnesium K X-rays in iron.

In the sodium case, there is a modest difference relative to the Part I calibration, but, having data from only feldspars (AL-I and FK-N), we are not in a position to draw definitive conclusions. Moreover, we must suspect that for the low X-ray energies of Na and Mg, the effects of a sample surface that is not perfectly smooth may not be negligible.

For minor and trace elements, the agreement between the two data sets is quite good. The overlap of the weak phosphorus peak with the intense neighboring silicon peak detracts from the accuracy of results for this element when its concentration is small (~0.1 wt.%); therefore, we have not included the data from GL-O and Mica-Fe in Table 5. In the case of chlorine, there is marked disagreement with the homogeneous standards of Part I. Chlorine could substitute for OH in three of the minerals concerned (UB-N, Mica-Fe, and Mica-Mg), in which case we would posit a homogeneous matrix and hence expect an *R*-value ~ 1; this is not what we observe, suggesting that the chlorine is present in trace impurities. In albite the chlorine must be in a trace impurity phase, in which case the computed matrix term for the GRM would differ strongly from that of the host phase, causing the observed discrepancy. For nickel, three of the pertinent four GRMs have very large uncertainties arising from the very low concentrations, but for UB-N (with Ni concentration 0.2 wt.%) the *R*-values is 1.01 ± 0.05. This probably reflects the fact that in serpentine, nickel substitutes for magnesium and iron, and is thus part of a homogeneous matrix.

Overall then, the agreement between the mono-mineralic GRMs and the homogeneous standards is at the 1% level for iron and silicon, a few percent for other major elements, and ~10% for minor and trace elements (with large uncertainty estimates here). No compelling reason emerges to alter the *H*-value that was determined from the homogeneous standards in Part I or to alter that overall calibration. There are two evident discrepancies in chlorine and magnesium. The latter demands further attention, as does the manner in which the aluminum data fall into two sub-groups, one showing excellent agreement and one showing a ~10% discrepancy which appears significant relative to the uncertainties that are attached to our *R*-values.

An argument could be made at this juncture to blend the mono-mineralic GRMs into the set of homogeneous standards. But, given the two open issues for magnesium and aluminum in the phyllosilicates, and the uncertainties attached to the data points for sodium, phosphorus, sulfur and chlorine, we shall refrain from this step until after a detailed consideration of the remaining GRMs, which are mostly igneous rocks. It would be useful in a future APXS calibration to expand the set of mono-mineralic GRMs to include more of the minerals that comprise the phases in igneous rocks.

7. Results from fixed-matrix analysis of the multiple-mineral rock GRMs

Table 6 summarizes error-weighted mean *R*-values, separated by rock type, for six major elements where variations among rock type are observed. Table 7 collects the mean *R*-values for all the other elements. Uncertified GRMs are excluded from calculation of these means. The quoted uncertainties in the mean *R*-values are the standard deviations within the rock sub-group concerned. For the two elements (iron and silicon) where we have the most data, the smallest individual error bars and the least scatter, we have adopted the estimated error of the mean as the uncertainty.

For the sediment material MAG-1, we have a pair of entirely distinct samples; the first of these was part of the suite prepared by Gellert et al. [2], and the second was one of the blind samples supplied by NASA. For the major elements (concentration > 1 wt.%), the average difference was only 2%; for the four minor and trace elements, the differences were in the range ±10%. This single case of duplication provides a useful indication of reproducibility. We derived our *R*-values from the means of the two concentration sets. Using the certified concentrations, the silicon *R*-value of 1.11 was the most extreme silicon outlier. A possible explanation is that

Table 6
Mean *R*-values (with one standard deviation) for major elements in the GRMs. Results from the homogeneous standard calibration of Part I are shown for comparison. Bold type indicates those cases where a departure of 10% or more from the homogeneous standard calibration suggests significant distortion of the matrix term calculation due to mineral phase heterogeneity.

	Na	Mg	Al	K	Ca	Fe
Hom Cal	0.88 ± 0.04	0.96 ± 0.04	1.01 ± 0.03	0.98 ± 0.01	1.01 ± 0.01	1.00 ± 0.004
Mineral GRMs	0.95 ± 0.03	0.84 ± 0.05	0.97 ± 0.03	0.99 ± 0.04		1.00 ± 0.02
Basalts	**1.18 ± 0.08**	0.87 ± 0.05	**1.17 ± 0.035**	1.00 ± 0.03	1.02 ± 0.035	0.97 ± 0.01
Andesites	1.00 ± 0.09	0.83 ± 0.15	1.03 ± 0.06	0.99 ± 0.015	1.015 ± 0.045	0.97 ± 0.025
Rhyolites	0.95 ± 0.05	0.93 ± 0.05	1.04 ± 0.03	1.06 ± 0.04	1.06 ± 0.015	0.96 ± 0.06
Trachytes	0.91 ± 0.02	**0.44 ± 0.02**	1.02 ± 0.015	1.01 ± 0.05	**0.84 ± 0.03**	**0.77 ± 0.04**
Anorthite	**1.10 ± 0.06**	0.93 ± 0.06	1.025 ± 0.02		1.07 ± 0.015	0.99 ± 0.02
Tephrite	0.98 ± 0.02	**1.35 ± 0.05**	1.07 ± 0.02	**1.14 ± 0.02**	**1.16 ± 0.02**	0.93 ± 0.01
Sediments	0.91 ± 0.21	1.07 ± 0.01	**1.13 ± 0.06**	1.02 ± 0.03	1.01 ± 0.035	0.985 ± 0.03

Table 7
Further mean *R*-values (with one standard deviation) for elements in the GRMs.

Element	Mean wt.%	*R* for group ± 1sd	Special cases
Si	24.5	1.011 ± 0.006	
P (igneous rocks only)	0.28	1.26 ± 0.14	
S	0.22	0.95 ± 0.30	
Cl	0.035 (omit MAG-1)	1.18 ± 0.20	MAG-1: 0.90 ± 0.18
Ti	0.94 (omit trachyes)	0.92 ± 0.05	Trachytes: 0.66 ± 0.03
Cr	0.065	1.11 ± 0.10	
Mn	0.11	1.08 ± 0.04	
Ni	0.013	1.03 ± 0.17	UB-N: 1.01 ± 0.05
Cu	0.019	1.3 ± 0.3	
Zn	0.035	1.06 ± 0.07	
Ga	0.005	0.99 ± 0.19	
Br (SY-4)	0.024	1.18 ± 0.06	MAG-1: 1.03 ± 0.3
W	0.016	1.00 ± 0.15	MA-N: 0.75 ± 0.06
Pb	0.020	1.1 ± 0.3	

the carbon may actually be present in organic matter, and has been released during the pre-heating of the sample. With the certificate value of 7.8 wt.% of CO_2 deleted from the matrix, this outlier and others become consistent with the results from other GRMs.

Plots of *R*-values versus concentration were presented in Ref. [4] for all the elements. It follows that only a sampling need be provided here, and our selection is influenced by our extension of the GRM suite. Interpretation of apparent anomalies is delayed until Section 8. The plots are in Figs. 3–8. To economize on the number of different symbols, we have combined picro-basalts and basalts under the basalt category, basaltic andesites and andesites under the andesite category, and dacites and rhyolites under the dacite category. Open symbols denote the four added GRMs which lack certification as defined in Section 2. The MPIC andesite results follow the same behaviour as that of the certified andesite GRMs. The uncertified trachyte results show behaviour not encountered before with the other rock types.

7.1. Major elements

For silicon (see Fig. 3), the overall mean *R*-value for all the GRMs is 1.011. The standard deviation of the data is ±3.2%; much of this variability might be attributed to small variations in the distance from the powder sample surfaces to the APXS. With an approximate distance of 30 mm, a variation of just ±0.3 mm causes a variation of ±2% in solid angle and hence in counting rate and in derived concentration. If we consider the silicon data to comprise a single population, the standard error of the mean *R*-value is ±0.006.

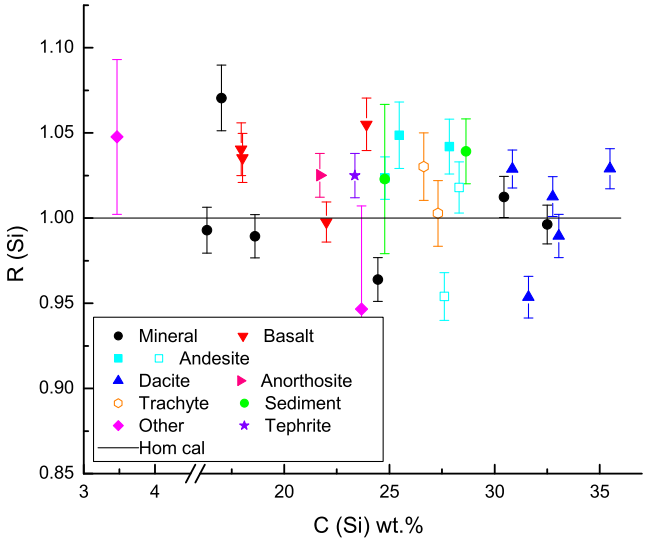

Fig. 3. *R*-values for silicon in the GRMs; the line is the mean *R*-value from the calibration of Part I; the line is the mean R-value from the calibration with homogenous standards in Part I.

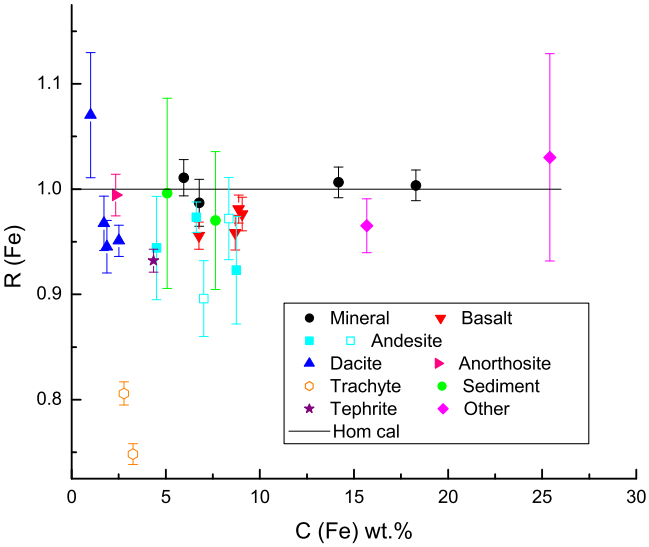

Fig. 4. *R*-values for iron in the GRMs; the line is the mean *R*-value from the calibration with homogenous standards in Part I.

For iron (Fig. 4), the only results which are strongly anomalous are those of the two trachytes. With the latter deleted, the weighted mean *R*-value is 0.972 with standard deviation 3.2%.

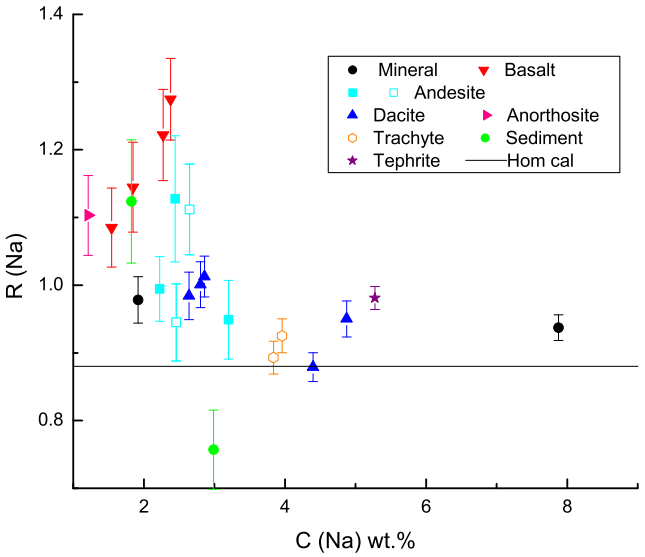

Fig. 5. *R*-values for sodium in the GRMs; the line is the mean *R*-value from the calibration with homogenous standards in Part I.

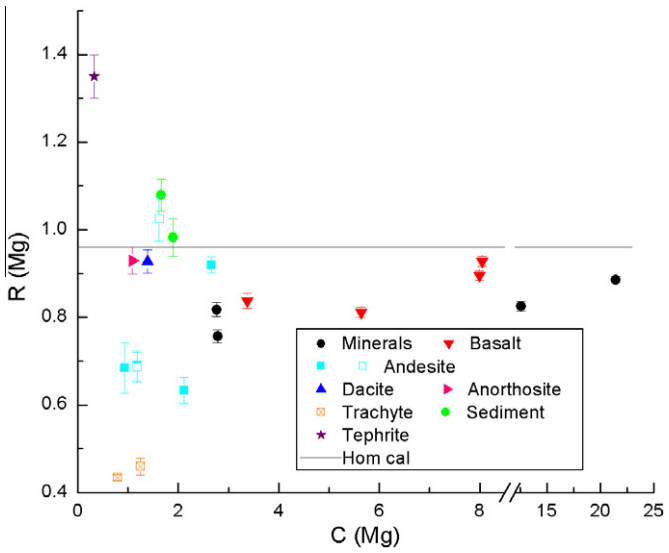

Fig. 7. *R*-values for magnesium in the GRMs; the line is the mean *R*-value from the calibration with homogenous standards in Part I.

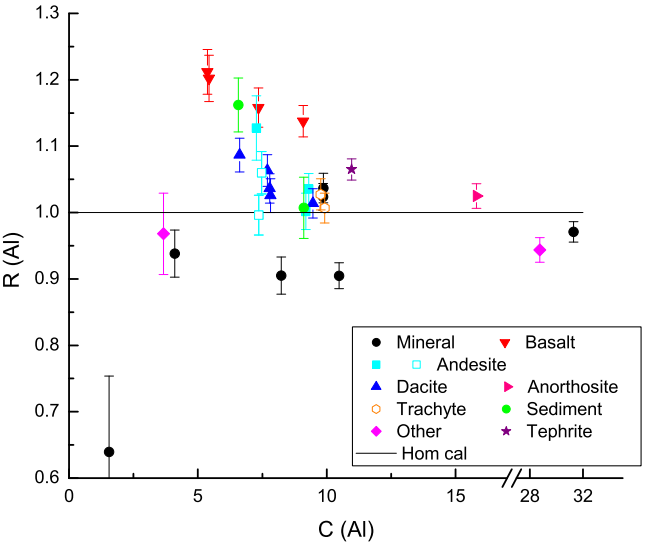

Fig. 6. *R*-values for aluminum in the GRMs; the line is the mean *R*-value from the calibration with homogenous standards in Part I.

The fact that this spread is identical to the silicon case reinforces the idea that the spread is dominated by sample placement variations. The *R*-value is 2.8% below our expected value from the calibration of Part I. Noting that the seven mono-mineralic GRMs had a mean *R*-value of 1.010 ± 0.016 (sem), in good agreement with the Part I calibration, we can remove these, and then observe that the mean *R*-value for the remaining seventeen rock GRMs is 0.961 ± 0.035 (sd). These results suggest the possibility of a small difference between the mono-mineralic and the rock GRMs as far as iron is concerned.

The sodium and aluminum data for the basalt, andesite and dacite sub-groupings exhibit the dependence upon rock type to which we drew attention in Ref. [4], as shown in Fig. 5 for the case of sodium. The appearance of this same effect in aluminum argues against the suggestion that the sodium effect might be a spectrum fitting phenomenon reflecting the proximity of the sodium peak to the low-energy cut-off of the spectrum. Fig. 6, for aluminum, serves the additional purpose of displaying the analogous UB-N datum, and the low R-values for the sheet silicate sub-group of the seven mono-mineralic GRMs.

For magnesium (Fig. 7), there are three extreme outliers, viz. the two trachyte results, which fall very low, and the tephrite result, which is very high. The basalt, andesite and mineral GRMs form a consistent sub-grouping, with an overall mean *R*-value of 0.86 (sd 0.09) which is rather lower than the expectation from Part I. The consistency between the basalt and andesite results on the one hand and the mineral GRM data on the other suggests that there is a common effect that conspires to lower the magnesium *R*-value, but we have not identified what this effect is.

The potassium and calcium (Fig. 8) results are overall in good agreement with expectations from Part I. The only anomalies are the high values for both elements in tephrite, and the two low calcium values in the trachytes. The weighted means of the potassium and calcium data points with the noted outliers excluded are in satisfactory agreement with the calibration of Part I.

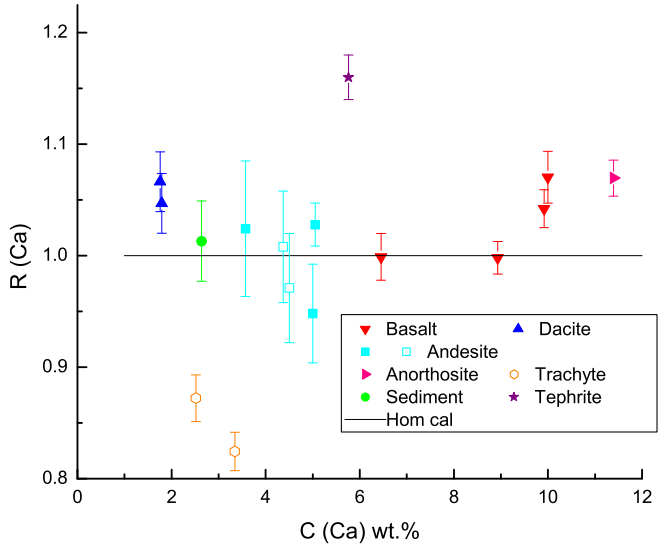

Fig. 8. *R*-values for calcium in the GRMs;

7.2. Minor elements titanium, manganese and zinc

In the titanium data, the mineral DT-N and the two trachytes (see Table 6) stand out as anomalous, departing significantly and in separate directions from the overall trend of the igneous rocks If we choose to exclude these three cases, we have a mean *R*-value of 0.92 (sd 0.1). The uncertainties on the two sediment data points are very large, but the mean *R*-value is unchanged if they are excluded. Presumably the difference between the mean value and that expected from Part I can be attributed to the fact that titanium is invariably in an accessory phase in these GRMs. With manganese and zinc, the uncertainties are quite large, and no rock-dependent trends are discernible. The mean *R*-values across all the GRMs agree within uncertainty with those of Part I.

7.3. Minor and trace elements phosphorus, sulfur, chlorine and bromine

Within large uncertainties, the phosphorus *R*-values are consistent across the igneous rocks, with a mean that is 43% higher than the homogenous calibration value of Part I. The very large uncertainties in the sulfur case preclude any definitive conclusions regarding that element. Turning to chlorine, thirteen of the GRMs have similar, very low chlorine levels, with an average of 0.04 wt.%; their weighted mean *R*-value is 1.18 ± 0.20. The fourteenth (tephrite) has ten times higher chlorine concentration, viz. 0.45%; its *R*-value of 1.21 is entirely consistent with the others, albeit within its large associated uncertainty. This high value is consistent with the result from the mono-mineralic GRMS, suggesting a common cause across the two groups. The MAG-1 sedimentary material, with 3.1 wt.% of chlorine, has $R = 0.9 \pm 0.2$; this large uncertainty, which reflects mainly the uncertainty in the certificate concentration value, suggests caution in drawing any conclusions.

Given the analogous case of chlorine, where the mean GRM *R*-value exceeded the homogenous calibration value by over 20%, we might expect similar behavior in bromine. For bromine, the work of Gellert et al. [2] had only a single GRM (MAG-1); the USGS assigns no uncertainty estimate to the certified concentration of 250 ppm wt., while the Los Alamos National Laboratory Geostandards website [31] assigns ± 28%. With this value, our result is $R = 1.03 \pm 0.3$. An independent study [32] of bromine in MAG-1 found concentrations of 311, 309 and 346 ppm wt. in three samples from one bottle, and 266 ppm wt. from a second bottle, implying a large variation among samples. In the present work, we have added data from the SY-4 standard, whose certificate indicates a bromine content of 217 ± 14 ppm wt., resulting in $R = 1.18 \pm 0.06$. These numbers may be compared with the mean *R*-value of 0.99 from the three bromine-bearing chemical standards. We deduce that the bromine R-value in SY-4 exceeds the calibration value of Part I.

7.4. Other trace elements

Chromium, nickel, copper, gallium, tungsten and lead are present as trace elements, and occur in only small subsets of a few GRMs. Their mean concentrations are very small, as seen in Table 6. The standard deviations of the mean *R*-values are therefore large, and no dependencies upon the rock type can be discerned. For lead, the increase in *R*-values at the lowest concentrations suggests that there is a very small concentration offset, although our effort in Section 3 above to determine that quantity gave a result consistent with zero. If we confine ourselves to those GRMs with concentration exceeding 0.005 wt.%, we have a mean *R*-value for lead of 1.1 ± 0.3. A few elements are detected in only one or two of the GRMs, an example being barium in Mica-Mg, where we find $R = 1.12$.

7.5. Sum of concentrations

GUAPX converts its output file of element concentrations to oxide concentrations (where appropriate) using normal stoichiometry; a few elements such as chlorine and bromine remain independent. It then sums all of these constituents to provide a total concentration of visible elements and oxides. We used Table 6 to create values of the empirical correction factors $k(Z)$ for the various rock types, and then ran GUAPX, incorporating these corrections. Barring unrecognized errors, we would expect that the ratio of this total visible concentration to the corresponding certificate value, which we shall refer to as *RTVC* (ratio of total visible concentrations) should be 1.0. For the minerals and igneous rocks which are not marked by asterisks in Table 1, the mean value of *RTVC* is 1.012 ± 0.023 (sd), in good agreement with expectation. Note that we excluded SY4 and ANG because in these cases we considered that one representative of a rock type was insufficient to determine $k(Z)$.

In contrast, for the six GRMs marked by asterisks in Table 1, a somewhat different result emerges. Four of these are the phyllosilicates Mica-Fe, Mica-Mg, glauconite (GL-O) and serpentine (UB-N), in which water is bound into specific layers within their overall crystal structures. The remaining two are the rocks bauxite (BX-N) and jasperoid (GXR-1), which have very large amounts of bound water; in the former it is present within the three aluminum hydrates (gibbsite, boehmite, and diaspore) which are the principal constituents. For these six cases, the mean *RTVC* value is 0.956.

However, before any conclusions are reached, the above results must be modified to reflect the split between FeO and Fe_2O_3 in the iron oxide component. In converting the iron concentration to oxide concentration, GUAPX assumes the default oxide form FeO. Inevitably, this incurs a small error in those cases where a portion of the oxide is in fact Fe_2O_3. When an unknown sample is being analyzed on Mars, there is no alternative to this approach, except when Mössbaüer spectroscopy data are available (as in the MER mission case) to provide the ferrous-to-ferric ratio. In the present study of standards, this information does exist in the supplier's certificate, and it can be applied as a final correction to the results of the two paragraphs above. For the first eighteen GRMs, the mean RTVC value increases by a negligible amount to 1.015. For the six water-bearing GRMs, the result becomes 0.972. This result could be taken to imply that the X-ray invisible components have higher concentrations than the certificate values, which in turn might suggest incomplete removal of the H_2O-component. Alternatively it may simply reflect the uncertainties in the *k*-values.

8. Interpretation of rock GRM results

The two trachytes ISH-G and MDO-G provide a convenient starting point for this discussion. From the XRD, these are predominantly plagioclase with a minor (13 wt.%) clinopyroxene component. The matrix terms for interactions of the exciting radiations in the minor pyroxene phase are very different from the matrix term that is actually computed by GUAPX on the assumption of a fully homogeneous distribution of atoms within an overall matrix. We might therefore expect the APXS analysis to be inaccurate for those elements that are confined to the minor pyroxene phase. This is the case, insofar as the magnesium and titanium *R*-values results fall very low. The calcium, sodium and iron *R*-values also fall low, but less dramatically, reflecting the fact that these elements are shared between the two main phases.

AN-G is also predominantly plagioclase, with the low sodium and potassium concentrations suggesting it is calcic plagioclase. But there is no pyroxene component and the iron *R*-value is not anomalous. The sodium *R*-value is higher than expected, but this

particular GRM shows the lowest sodium concentration (1.3 wt.%) of all those examined; given the consequent small size of the peak and the uncertainty in fitting the extreme lower end of the spectrum, we think it would be unwise to draw any conclusions about mineral phase effects in this case.

We see the opposite situation to the trachytes in the basalt BE-N, where the presence of 30 wt.% of nepheline and gonnardite (alkali aluminosilicates) suggests that the sodium and aluminum are present predominantly in these phases, as opposed to the 61 wt.% pyroxene (Mg, Ca, Fe silicate) and olivine (Mg, Fe silicate) phases. The gonnardite could well be an alteration phase produced by breakdown of the precursor nepeheline, primarily through interaction with water. The matrix terms will be dominated by the pyroxene and olivine, and will therefore be inaccurate for the elements in the minor minerals. In this case then, we might expect significantly better results for iron and magnesium together with anomalies for sodium and aluminum. The *R*-values for the latter two elements are indeed ~20% high, while those for magnesium and iron show no irregularities.

In our earlier work [4] we observed that this anomalous behaviour of the sodium and aluminum results continued, but with steadily diminishing strength, as one proceeds through the rock sequence basalts–andesites–dacites–rhyolites, i.e. along the silica content axis of the simplified LeMaitre diagram. However, there was considerable scatter among the andesite results. With the addition of two more andesite standards, and new information from the XRD work, we now see that the dependence of the effect upon SiO_2 concentration is a manifestation of a more complex cause. As the SiO_2 content increases along the basalt–rhyolite sequence, the concentration of the iron-bearing minerals pyroxene and olivine also decreases, as is demonstrated by the XRD results of Table 3. We have therefore plotted the *R*(Al) and *R*(Na) values for this sequence of rock GRMs against the iron concentration in Figs. 9 and 10. Clearly, there are two factors at play in influencing these *R*-values: (i) the increasing content of iron-containing phases; (ii) the very high attenuation coefficients for sodium (8260 $cm^2\ g^{-1}$) and aluminum (2320 $cm^2\ g^{-1}$) K X-rays in iron.

Although Jsd2 is a stream sediment standard and is not classified as an igneous rock, we include its results in Figs. 9 and 10. From Table 3, we see it contains 34 wt.% of pyroxene and 39 wt.% of plagioclase. This high pyroxene content suggests that we should see similar behaviour of its sodium and aluminum results to the basalt results. This precisely what is observed in Figs. 9 and 10, lending further support to the arguments of the previous paragraph.

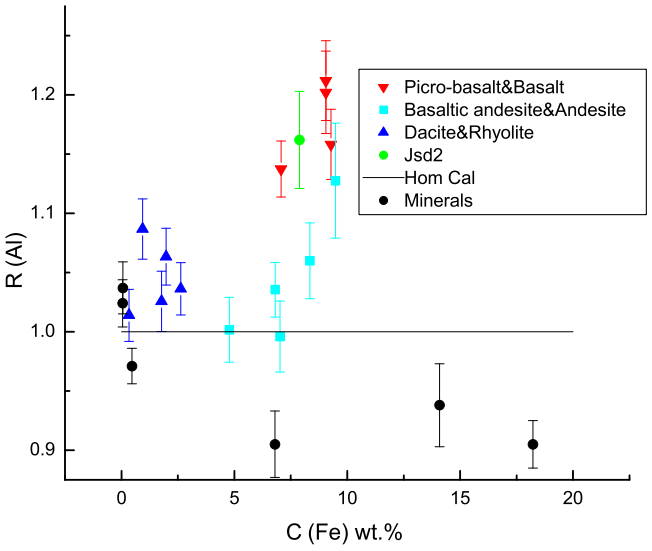

Fig. 9. *R*-values for aluminum plotted versus iron concentration in the GRMs; the line is the mean *R*-value from the calibration with homogenous standards in Part I.

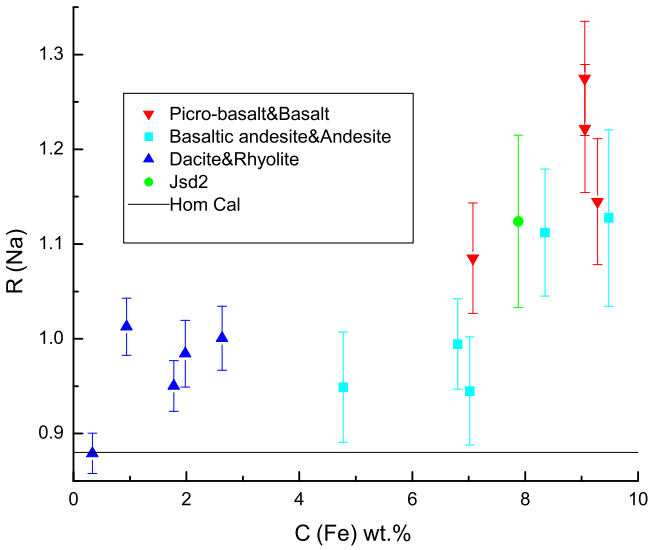

Fig. 10. *R*-values for sodium plotted versus iron concentration in the GRMs; the line is the mean *R*-value from the calibration with homogenous standards in Part I.

On the basis of the above mineral phase arguments, potassium would be expected to show similar effects to sodium and aluminum in this rock sequence., but it does not, possibly reflecting the much lower attenuation coefficient (428 $cm^2\ g^{-1}$) of its K X-rays in iron, and also the fact about 40% of these X-rays arise from XRF as opposed to PIXE. If grain sizes are very small, then the PIXE-induced X-rays of the lightest elements will only encounter the matrix of the mineral phase in which they originate; but with increasing atomic number and longer X-ray path lengths, X-rays may pass through more than one phase en route to detection.

The arguments above strongly support the contention that anomalous *R*-values arise when two conditions are satisfied: (i) the element concerned is located predominantly in an accessory or minor phase and (ii) the dominant phase contains one or more elements that are highly absorbing for the X-rays of the element under study. In the GRMs discussed so far, the main absorbing element in the major phase has been iron. The dacite and rhyolite GRMs contain iron at levels 0.3–2.6 wt.%, and the mean *R*-value (0.98) is very close to unity. Their predominant mineral, plagioclase, can contain such levels of iron in solid solution; as cooling of the initial melt proceeds, the ability of the feldspar structure to contain iron decreases, frequently leading to the exsolution of a Fe-bearing phase such as ilmenite ($FeTiO_3$), but we have no XRD evidence for ilmenite. The most likely host of the iron is then fine-grained oxides. Our excellent *R*-value for iron in dacites and rhyolites reflects the fact that the major phases of these GRMs contain only small quantities of elements which could strongly absorb the iron K X-rays from minor phases.

The titanium mean *R*-value, exclusive of the three anomalies (DT-N and two trachytes) mentioned earlier, is 0.92. We dealt above with the trachyte anomaly. This leaves the mineral DT-N as the only case where the Ti *R*-value of 1.14 ± 0.07 is significantly above the mean. In the DTN (kyanite, Al_2SiO_5), the XRD identification of rutile (TiO_2) indicates that this mineral hosts the titanium. In all the other GRMs, significant concentrations of potassium and calcium are present, which are strong absorbers of Ti K X-rays. This difference may explain the DT-N anomaly.

Our anomalous mean *R*-value for phosphorus in basalts, andesites and rhyolites points to the phosphorus being present as an

accessory phase, and indeed this is generally the case, with apatite or whitlockite being the host.

Apparent anomalies in the tephrite *R*-values are of a more complex nature. The dominant mineral phases are plagioclase and scapolite. The high result for magnesium can be attributed to it being in accessory biotite. The 10 wt.% calcite datum from the XRD coupled with the certificate calcium concentration suggests that most of the calcium is present in the calcite. In turn, this suggests that the plagioclase component sits towards the sodium end of the sodium-calcium series, and similarly for the scapolite (a sodium, calcium alumino-silicate). The anomalously high calcium *R*-value can be attributed to the calcium K X-rays arising mainly from calcite (in which they are only weakly attenuated) whereas the matrix term is dominated by plagioclase and scapolite. The good *R*-values for sodium and aluminum reflect that these elements are located in the major phases. We do not have an explanation for the high *R*-value of potassium.

9. Analysis of unknown samples

In the case of unknown samples, it is obvious that the fixed-matrix method for solving Eq. (1) is inapplicable; it was developed specifically for calibration purposes as detailed above. Moreover the sample-APXS geometry varies on Mars, and hence the determined *H*-value will no longer apply, although the $k(Z)$ corrections will. It follows that Eq. (1) now must be solved in an iterative fashion, with the element concentrations iterated to consistency subject to having a total visible concentration (oxides and elements) of 100 wt.%. We have recently shown in detail [29] that when this iterative-matrix (IM) approach is tested on the GRMs, it provides essentially the same results as the FM approach provided that the concentration of X-ray invisible elements is less than ~3 wt.%. But larger X-ray invisible contributions cause significant error, because in the IM mode GUAPX is unaware of their presence; it therefore excludes them from the normalization to 100 wt.%, and makes erroneous matrix corrections that neglect the effects of the water. Taking UB-N for example, this causes the concentrations of magnesium, silicon and iron to be erroneously increased by factors of 1.12, 1.17 and 1.24 respectively. It follows that the IM mode should not be employed for calibration purposes if GRMs contain significant concentrations of X-ray invisible components.

We now examine the matter of determining from our *R*-values (see Section 5) a set of empirical correction factors $k(Z)$ to be inserted in Eq. (1) for the IM analysis mode that is pertinent for unknown samples. In the coarsest of these approaches, the *k*-value for a given element would be set equal to the mean or median *R*-value for that element across the entire suite of GRMs. If all rock types are to be included, an uncertainty will have to be assigned to $k(Z)$ which reflects the entire range of *R*-values for that element. Such an uncertainty in some cases (see Tables 6 and 7) is very large. But if outliers are excluded in order to reduce this uncertainty, then some rock types would then be automatically excluded, leading to inaccurate analyses. Examples of this would be the exclusion of the basalt values for $R(\mathrm{Na})$ or the trachyte values for $R(\mathrm{Mg})$.

Our preferred alternative approach in real analysis would include two stages. The first stage would be the coarse analysis described above. Its results, together with any ancillary information from other instruments, would then be used to estimate what might be the possible mineralogical composition of the sample. For example, this might tell us that the sample is most likely basalt. In the second stage, the iterative-matrix analysis would be repeated using a set of $k(Z)$ values derived from the basalt calibration data of Table 6 or its equivalent. We tested this refined approach in some detail in Ref. [29] by separating out single GRMs from the suite of Table 1 and treating them as unknown samples measured in the same geometry as the "standards". With the exception of the six water-bearing GRMs that are marked by asterisks in Table 1, the RTVC values were within 1–2% of unity, and the element concentrations were in very good agreement with the certificate values. In these six water-bearing cases, the arguments laid out in Section 7 above hold again. When information on X-ray invisible components is unknown or deliberately withheld (as a test), the iterative solution mode yields erroneous results in samples having significant X-ray invisible content.

Of course, if analyses on Mars were to be performed in precisely the same geometry as was used for the laboratory calibration, the normalization to 100 wt.% would be unnecessary. In that special case, any shortfall, relative to 100 wt.%, of the summed oxide and element concentrations would directly suggest the presence of X-ray invisible elements. For this reason, GUAPX allows the user to include one specified X-ray invisible component (e.g. H_2O+) within the matrix: this component is rigorously included in computation of the matrix term, and its concentration is determined as the difference between 100 wt.% and the sum of the visible element and oxide concentrations. We tested this through use of the phyllosilicate UB-N. If we fit this spectrum as an unknown sample, using appropriate *k*-values and including H_2O+ as an invisible component, the H_2O+ concentration emerges as 11.85 wt.% after applying the iron oxide correction. This agrees very well with the sum of 10.8 wt.% H_2O+ and 0.4 wt.% CO_2 given on the supplier's certificate. However, the relative uncertainty (1sd) of the magnesium *k*-value is ±10%, and this translates to a ±30% relative uncertainty in our water result. It is seen that the accuracy of water determination depends strongly upon the accuracy of the element calibration, as expected.

This demonstrates an interesting potential of the APXS, which has not been exploited to date. If a means of determining the sample-APXS distance precisely were added to future instruments, the appropriate *H*-value could be determined by a simple geometric normalization of the terrestrial *H*-value, and determination of X-ray invisible components would become a possibility.

10. Conclusions

The objectives laid out for this paper and its predecessor (Part I) have been attained. In Part I, a calibration of the MER APXS has been achieved through use of only simple chemical and mineral standards which are homogeneous in the sense that they contain only a single chemical phase. The internal consistency of this calibration reflects the good quality of the database that is used by GUAPX. Issues do remain, however. Lack of knowledge of incomplete charge collection effects in the X-ray detector precludes incorporating these in our detector model, and forces us into reliance on the measurements alone for the elements phosphorus, sulfur and chlorine. We do not have a full understanding of the measured *R*-values for magnesium and aluminum, and more work is needed to ascertain if the sheet structure of phyllosilicates plays a role here.

In this paper, we have probed the degree to which a diverse set of geochemical reference materials supported the above calibration. The agreement was quite good but far from perfect. Systematic divergences were observed for specific elements in specific igneous rock types as defined in a LeMaitre diagram. Some elements, e.g. phosphorus, chlorine and bromine, were markedly anomalous in all the rock GRMs. Most, but not all, of these effects were attributed to the location of elements within major, minor and accessory mineral phases, a natural effect which is at variance with our method's necessary assumption (shared with the method of Gellert et al. [2]) that the matrix is homogeneous in elemental

distribution at the sub-micron scale of distances. The basic point here is that the matrix terms in Eq. (1) are determined by assuming that the elements are homogeneously distributed in the sample, and are thus, in some sense, an average over all the mineral phases that are present; obviously then, they are determined principally by the major mineral phase, and will inevitably be inaccurate for those elements which are located in a minor phase, and even more so when they are in an accessory phase. One example of this is the positive deviations seen for sodium and aluminum in basalts; these elements occur in minor, felsic phases while the major phase is typically pyroxene or olivine. Inclusion of the trachyte GRMs in the present work proved to be very valuable here, because these rocks present the opposite situation, with a major feldspar phase and a minor pyroxene phase. In this case, good results are obtained for sodium and potassium while the iron, magnesium and calcium in the accessory phases show large negative deviations. The symmetry of these results supports our invocation of mineralogical phase effects as the cause of the observed deviations.

Various cautionary notes must be drawn from this evidence. If the APXS calibration is effected by some sort of averaging over a GRM suite that includes many rock types, then our present results show that a smooth interpolation as a function of atomic number to handle "missing" elements cannot be justified. Moreover, some combinations of rock type and elements will appear to be outliers, and will be at risk of rejection from the calibration scheme. The merit of separating the standards into one sub-group of homogeneous standards and a second sub-group of GRMs, and considering the two sets of results separately has been clearly demonstrated here. In actual analysis of rock types whose mineralogy has not been identified, large errors can arise even for major and minor elements.

On the positive side, using the GRM results enabled us here to develop a limited set of "sub-calibrations" which are tuned to different rock types. If a preliminary coarse APXS analysis coupled with ancillary information can identify the rock type, then a second GUAPX run with a sub-calibration tuned to that rock type can provide more refined and accurate results. It is desirable to develop this concept further by expanding the range and number of GRMs studied, and this is being done in the calibration of the Mars Science Laboratory APXS, which is currently in progress at the University of Guelph. This work will enable us to ascertain whether or not more of LeMaitre's rock classifications [6] can be used to focus our sub-calibrations more finely according to rock type. It is hoped that this work might also resolve new issues that have arisen here such as the apparent departure of light element *R*-values in sheet silicates from those of framework silicates.

Other useful issues surfaced during the work. The value of having a Mössbaüer spectrometer to determine the Fe^{2+}/Fe^{3+} ratio was underlined by the observed interplay between the stoichiometric conversion of measured iron to its oxide and the possibility to measure the content of bound water or other X-ray invisible material such as carbonate. It was shown through use of the phyllosilicate material UB-N that the latter measurement is indeed feasible, but it would only be useful on Mars if additional instrumentation was developed to enable precise and accurate measurement of the distance between the sample and the APXS. Such an enhancement should be considered in APXS design for future planetary missions. This approach to measuring water content demands the best possible accuracy in the determination of the $k(Z)$ factors, which in turn demands an expanded set of GRMs, optimum detector energy resolution, accurate spectrum fitting, and a rigorous approach to the determination of matrix terms via fundamental parameters.

Acknowledgements

This work was supported in part by the Natural Sciences and Engineering Research Council of Canada. S. Taylor was partly supported by the Ontario Centres of Excellence. We are very grateful to R. Rieder for introducing us to the challenge of APXS calibration, and to R. Gellert for provision of the calibration spectra, continuing collaboration and excellent advice. We thank J. Crisp (NASA) for kindly providing information on five blind samples.

References

[1] J.L. Campbell, B.N. Jones, W. Brown-Bury, J.A. Maxwell, A GUPIX-based approach to interpreting the PIXE-plus-XRF spectra from the Mars exploration rovers: II geochemical reference materials, preceding paper.
[2] R. Gellert, R. Reider, J. Brückner, B.C. Clark, G. Dreibus, G. Klingelhöfer, G. Lugmair, D.W. Ming, H. Wänke, A. Yen, J. Zipfel, S. Squyres, Alpha particle X-ray spectrometer (APXS): results from Gusev Crater and calibration report, J. Geophys. Res. 111 (2006) JE002555.
[3] J. Brückner, G. Dreibus, R. Gellert, S. Squyres, H. Wänke, A. Yen, J. Zipfel (Mars exploration rovers: chemical composition by the APXS), in: J. Bell (Ed.), The Martian Surface, Cambridge University Press, 2008.
[4] J.L. Campbell, M. Lee, B.N. Jones, S.M. Andrushenko, N.G. Holmes, J.A. Maxwell, S.M. Taylor, A fundamental parameters approach to calibration of the Mars exploration rover alpha particle X-ray spectrometer, J. Geophys. Res. 114 (2009) JE003272.
[5] H.Y. McSween Jr., J. Taylor, M.B. Wyatt, Elemental composition of the Martian crust, Science 324 (2009) 736–739.
[6] R.W. LeMaitre et al., Recommendations of the International Union of Geological Sciences, Sub-commission of the Systematics of Igneous Rocks, Cambridge University Press, UK, 2002.
[7] J.A. Crisp, private communication from NASA, 2010.
[8] A. March, Mathematische theorie der regelung nach der korngestalt bei affiner deformation, Z. Kristallogr. 81 (1932) 285–297.
[9] W.A. Dollase, Correction of intensities for preferred orientation in powder diffractometry: application of the March model, J. Appl. Crystallogr. 19 (1986) 267–272.
[10] E. Prince, G. Donnay, R.F. Martin, Neutron diffraction refinement of an ordered orthoclase structure, Am. Mineral. 58 (1973) 500–507.
[11] G. Ferraris, D.W. Jones, J. Yerkess, A neutron-diffraction study of the crystal structure of analcime, NaAlSi2O6 H2O, Z. Kristallogr. Kristallgeom. Kristallphys. Kristallchem. 135 (1972) 240–252.
[12] P.E. Mackie, R.A. Young, Fluorine-Chlorine interaction in fluor-chlorapatite, J. Solid State Chem. 11 (1974) 319–329.
[13] S.R. Bohlen, D.R. Peacor, E.J. Essene, Crystal chemistry of a metamorphic Biotite and its significance in water barometry, Am. Mineral. 65 (1980) 55–62.
[14] H. Effenberger, K. Mereiter, J. Zemann, Crystal structure refinements of magnesite, calcite, rhodochrosite, siderite, smithsonite, and dolomite, with the discussion of some aspects of the stereochemistry of calcite-type carbonates, Z. Kristallogr. 156 (1981) 233–243.
[15] H. Zheng, S.W. Bailey, Structures of intergrowth triclinic and monoclinic lib chlorites from Kenya, Clay Clay Mineral. 37 (1989) 308–316.
[16] V.S. Urusov, O.N. Zver'kova, N.A. Yamnova, A.V. Polosin, Complex refinement of the structure of actinolite, Vestnik Moskovskogo Universiteta, Geologiya 42 (1987) 43–53.
[17] D. Pasqual, G. Molin, P.F. Zanazzi, G.M. Crisci, Clinopyroxene from Lipari: comparison with analogues from other Aeolian Islands, Italy, Can. Mineral. 36 (1998) 97–105.
[18] F. Mazzi, A.O. Larsen, G. Gottardi, E. Galli, Gonnardite has the tetrahedral framework of natrolite: experimental proof with a sample from Norway, Neues Jahrbuch fuer Mineralogie, Monatshefte (1986) 219–228.
[19] J.K. Winter, S. Ghose, Thermal expansion and high temperature crystal chemistry of the Al_2SiO_5 polymorphs, Am. Mineral. 64 (1979) 573–586.
[20] M.E. Fleet, The structure of magnetite: symmetry of cubic spinels, J. Solid State Chem. 62 (1986) 75–82.
[21] M.F. Brigatti, P. Frigieri, L. Poppi, Crystal chemistry of Mg-, Fe-bearing muscovites – 2M, Am. Mineral. 83 (1998) 775–785.
[22] R.J. Angel, G.D. Gatta, T. Boffa Ballaran, M.A. Carpenter, The mechanism of coupling in the modulated structure of nepheline, Can. Mineral. 46 (2008) 1465–1476.
[23] A. Hushur, M.H. Manghnani, J.R. Smyth, F. Nestola, D.J. Frost, Crystal chemistry of hydrous forsterite and its vibrational properties up to 41 GPa, Am. Mineral. 94 (2009) 751–760.
[24] W. Joswig, T. Tagai, M. Korekawa, H.R. Wenk, Verfeinerung der gemittelten Struktur eines Plagioklases An66 von der Insel Surtsey, Island, mittels Neutronenbeugung, Z. Kristallogr. Kristallgeom. Kristallphys. Kristallchem. 144 (1976) 433.
[25] R.M. Hazen, L.W. Finger, R.J. Hemley, H.K. Mao, High-pressure crystal chemistry and morphization of alpha quartz, Solid State Commun. 72 (5) (1989) 507–511.
[26] M. Okrusch, R. Hock, U. Schuessler, A. Brummer, M. Baier, H. Theisinger, Intergrown niobian rutile phases with Sc- and W-rich ferrocolumbite: an electron-microprobe and Rietveld study, Am. Mineral. 88 (2003) 986–995.
[27] E.V. Sokolova, E.R. Gobechiya, A.A. Zolotarev, Y.K. Kabalov, Refinement of the crystal structures of two marialites from the Kukurt deposit of the East Pamir, Crystallogr. Rep. 45 (2000) 934–938.
[28] R.A. Young, The Rietveld Method, International Monographs on Crystallography, 5, 1993.

[29] J.L. Campbell, S.M. Andrushenko, S.M. Taylor, J.A. Maxwell, A fundamental parameters approach to calibration of the Mars exploration rover alpha particle X-ray spectrometer: 2. Analysis of unknown samples, J. Geophys. Res. 115, E04009, doi:10.1029/2009JE003481.
[30] M. Omand, J.A. Maxwell, J.L. Campbell, Simulation of the relationship between elemental concentrations and X-ray yields in the Mars exploration rover's X-ray spectrometer, Nucl. Instr. Meth. B 229 (2005) 123–136.
[31] International Environmental Reference Materials, Los Alamos National Laboratory, <http://www.geostandards.lanl.gov>.
[32] W.J. Ullman, G. Tisue, Determination of bromine and iodine in USGS standard marine mud (MAG-1), Geostand. Geoanal. Res. 7 (2007) 289–290.